

# Machine learning via relativity-inspired quantum dynamics

Zejian Li,<sup>1</sup> Valentin Heyraud,<sup>1</sup> Kaelan Donatella,<sup>1</sup> Zakari Denis,<sup>1</sup> and Cristiano Ciuti<sup>1</sup>

<sup>1</sup> *Université Paris Cité, CNRS, Laboratoire Matériaux et Phénomènes Quantiques (MPQ), 75013 Paris, France*

(Dated: May 18, 2022)

We present a machine-learning scheme based on the relativistic dynamics of a quantum system, namely a quantum detector inside a cavity resonator. An equivalent analog model can be realized for example in a circuit QED platform subject to properly modulated driving fields. We consider a reservoir-computing scheme where the input data are embedded in the modulation of the system (equivalent to the acceleration of the relativistic object) and the output data are obtained by linear combinations of measured observables. As an illustrative example, we have simulated such a relativistic quantum machine for a challenging classification task, showing a very large enhancement of the accuracy in the relativistic regime. Using kernel-machine theory, we show that in the relativistic regime the task-independent expressivity is dramatically magnified with respect to the Newtonian regime.

*Introduction.*— Among several approaches for the conception of quantum computing devices, the field of relativistic quantum information [1, 2] has also emerged. It has been demonstrated that non-inertial motion, or, via the equivalence principle, gravitational fields, can be used to generate quantum gates. Recent theoretical works have demonstrated that a non-uniformly accelerated cavity can generate two-mode squeezing [3] and cluster states [4] for continuous-variable quantum computing [5]. In a complementary scenario, a cavity remains inertial, but hosts accelerated detectors. Also for this configuration it has been shown that universal single-qubit rotations can be performed [6]. While all the existing proposals for relativistic quantum computing require a very challenging control of mechanical motion, the corresponding models can be however synthesized in artificial platforms [7–9] such as those based on circuit QED [10] or trapped ions [11].

In recent years, *reservoir computing* has emerged as an appealing paradigm of information processing [12]. This framework consists in approximating a target function by feeding its arguments as an input of a *reservoir*, whose dynamics nonlinearly maps the data into a high dimensional space. The resulting output data are then fed into a parametrized linear transformation to yield a trial function. These parameters are finally optimized through supervised-learning. This architecture makes the computational resources involved in the training process relatively modest. This has led to proposals and realizations in diverse platforms, including free-space optics [13–15], photonics [16, 17], nonlinear polariton lattices [18–20], memristors [21, 22] and beyond [23–26]. Very recently, such an approach has been explored in a quantum context [27, 28], with applications in quantum metrology [29, 30], quantum-state control [31–33] and image recognition [34, 35]. Although it was long thought that a strong nonlinearity of the equations of motion was an essential element of reservoir computing, recent works have shown great performances relying on systems with almost no intrinsic nonlinearity, namely by exploiting the

nonlinearity of the measurement [15, 36, 37] or drawing links with approximate kernel evaluation [38–40].

In this letter, we present a reservoir-computing scheme exploiting the relativistic motion of a quantum system. We consider a paradigmatic model describing a quantum detector (atom) moving inside a cavity resonator. The relativistic dynamics can be simulated by an analog system such as a circuit QED platform with a tailored modulation of driving fields [8]. We explore the dynamics where the input data are embedded into the system by modulating the acceleration of the detector and measured output observables are then fed to a trainable linear classifier. By evaluating task-independent figures of merit, we demonstrate that the expressivity of our machine-learning protocol is dramatically enhanced in the relativistic regime. Moreover, we provide an illustrative example with a challenging classification task.

*Relativistic quantum model.*— Let us consider the model describing a quantum harmonic detector with proper frequency  $\Omega$ , minimally coupled to a quantum field  $\hat{\phi}$  inside an optical cavity. In the interaction picture, the corresponding Hamiltonian takes the Unruh-Dewitt form [41, 42]  $\hat{H}(\tau) = \lambda \hat{m}(\tau) \hat{\phi}[x^\mu(\tau)]$ , where  $\tau$  is the proper time of the detector,  $\lambda$  is the coupling constant, and  $\hat{m}(\tau) = \hat{b}e^{-i\Omega\tau} + \hat{b}^\dagger e^{i\Omega\tau}$  depends on the detector annihilation (creation) operator  $\hat{b}$  ( $\hat{b}^\dagger$ ). Finally,  $x^\mu(\tau) = (t(\tau), x(\tau))$  is the world line of the detector in the 1+1D Minkowski spacetime. We will adopt the metric  $\eta_{\mu\nu} = \text{diag}(+1, -1)$  and natural units such that  $\hbar = c = 1$ . For a multi-mode cavity with perfectly reflecting mirrors [6, 43],

$$\hat{H}(\tau) = \lambda \sum_{n=1}^{\infty} \frac{\sin[k_n x(\tau)]}{\sqrt{L\omega_n}} \times \left( \hat{b}\hat{a}_n e^{-i[\Omega\tau + \omega_n t(\tau)]} + \hat{b}\hat{a}_n^\dagger e^{-i[\Omega\tau - \omega_n t(\tau)]} \right) + \text{H.c.}, \quad (1)$$

where  $\omega_n = k_n = n\pi/L$  and  $L$  is the cavity length. The mode operators (denoting  $\hat{a}_0 \equiv \hat{b}$  for the detector) satisfy bosonic commutation relations  $[\hat{a}_n, \hat{a}_m^\dagger] = \delta_{nm}$ . Both

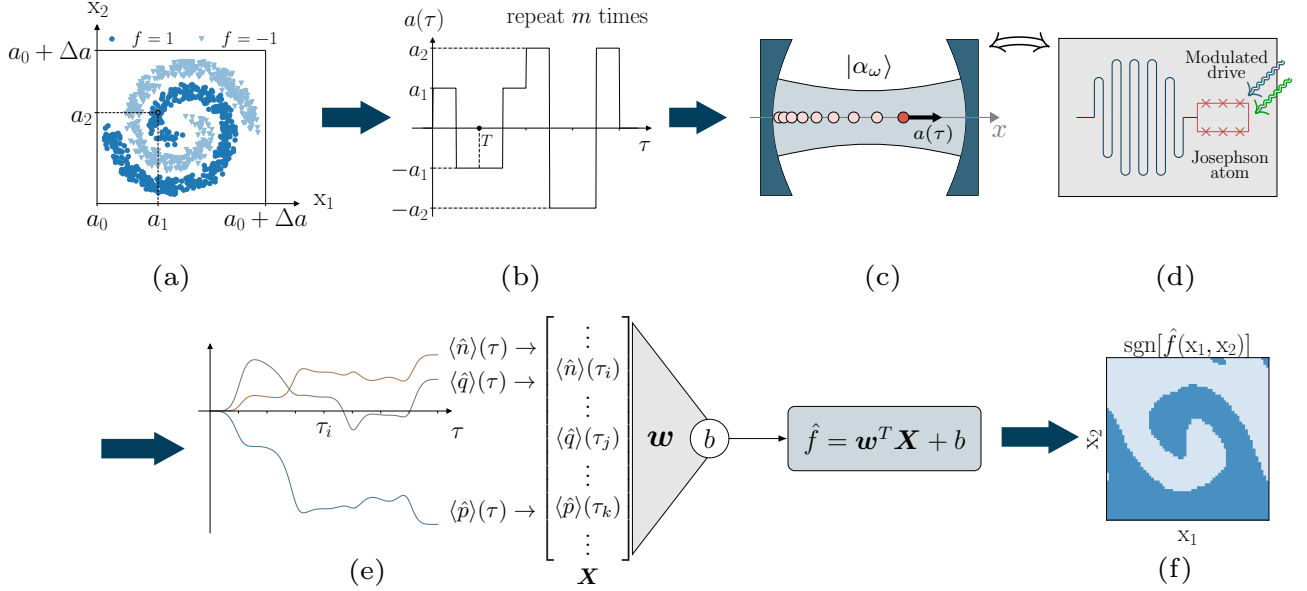


FIG. 1. Scheme of the relativistic reservoir-computing protocol. (a) Each point  $\mathbf{x} = (x_1, x_2)$  of the dataset is linearly mapped to acceleration values  $(a_1, a_2)$  according to Eq. (5). (b) The acceleration values are used to construct a piece-wise constant acceleration profile  $a(\tau)$ . (c) The quantum detector, initially at rest in the cavity prepared in a single-mode coherent state, undergoes non-inertial motion with proper acceleration  $a(\tau)$ . (d) Analog circuit QED system where the analogous of the proper acceleration is controlled by modulated driving fields. (e) Observables of the detector are measured at different times giving the feature vector  $\mathbf{X}$  and the affine trial function  $\hat{f} = \mathbf{w}^T \mathbf{X} + b$ . (f) The classification result is predicted by  $\text{sgn}[\hat{f}(x_1, x_2)]$ .

rotating and counter-rotating terms are present and contribute in the non-inertial regime [6].

Let us prepare the cavity in a single-mode coherent state whose frequency is resonant with that of the detector. Let us also consider the detector initially in its ground state  $\hat{\rho}_{0,(a)} = |0_a\rangle\langle 0_a|$ . The density matrix then reads:

$$\hat{\rho}_0 = \hat{\rho}_{0,(a)} \otimes |\alpha_{\omega_i}\rangle\langle \alpha_{\omega_i}| \bigotimes_{j \neq i} |0_{\omega_j}\rangle\langle 0_{\omega_j}|. \quad (2)$$

For a given  $x^\mu(\tau)$ , the time evolution of the density matrix is given by

$$\frac{d\hat{\rho}(\tau)}{d\tau} = -i[\hat{H}(\tau), \hat{\rho}(\tau)]. \quad (3)$$

Since all the considered modes are bosonic and the Hamiltonian is quadratic, the Gaussianity of the initial state is preserved during the evolution. The dynamics of  $\hat{\rho}(\tau)$  can therefore be solved exactly using the covariance-matrix formalism for Gaussian states [41, 44] [see Supplementary Material (SM) [45]].

*Circuit QED analog implementation.*— As shown in the literature [8], the Hamiltonian (1) can be implemented on a circuit QED platform consisting of an artificial Josephson atom [46] coupled to a multi-mode transmission line resonator [see Fig. 1(d)] [8]. For a single

mode, the Hamiltonian reads

$$\hat{H}^{\text{QED}}(\tau) = \omega_0 \hat{a}^\dagger \hat{a} + \epsilon \hat{b}^\dagger \hat{b} + \eta \zeta(\tau) \hat{b}^\dagger \hat{b} + g(\hat{b}^\dagger + \hat{b})(\hat{a}^\dagger + \hat{a}), \quad (4)$$

where  $\zeta(\tau)$  is the sum of four driving fields containing two different tones and two non-adiabatically modulated phases (see SM [45]). To get the equivalent of the acceleration range considered in this work, frequencies  $\omega_0$  and  $\epsilon$  can be taken in the standard GHz range while  $g$ ,  $\Omega$  and the phase modulation rates are in the MHz range (for more details, see SM [45]). This driving scheme gives rise to the same interaction-picture Hamiltonian as Eq. (1) for a single mode, and can be similarly extended to multi-mode circuit-QED systems [47–49]. While here we will report the results with a harmonic detector, we have also simulated the other extreme case where the Josephson atom is a *two-level system* and found similar results (see SM [45]), showing that the detailed atom spectrum is not crucial.

*Reservoir-computing protocol.*— Now, we can show how to exploit the relativistic system as a reservoir-computing model. The goal is to learn a nonlinear function  $f(\mathbf{x})$  of the input  $\mathbf{x} \equiv (x_1, x_2, \dots, x_N)$  that follows some probability distribution  $\mu(d\mathbf{x})$  (see Fig. 1). Assuming that for every  $i$  we have  $x_{i,\min} \leq x_i \leq x_{i,\max}$ , we map them linearly to acceleration values in a fixed range

between  $a_0$  and  $a_0 + \Delta a$ , namely

$$x_i \mapsto a_i = a_0 + \Delta a \times \frac{x_i - x_{i,\min}}{x_{i,\max} - x_{i,\min}}. \quad (5)$$

We then impose a piecewise constant proper acceleration  $a(\tau)$  to the harmonic detector. The pieces have proper acceleration values  $(a_1, -a_1, -a_1, a_1, \dots, a_N, -a_N, -a_N, a_N)$  and each piece has a duration of  $T/2$  in the proper frame of the detector, and we repeat this encoding sequence  $m$  times. Assuming the detector to be initially at rest at  $x^\mu(\tau = 0) = (t = 0, x = 0)$ , this acceleration profile guarantees that at each instant  $\tau = nT$ ,  $n \in \mathbb{N}$ , the detector is at rest, and that at  $\tau = 2nT$  it comes back to its original spatial position at  $x = 0$ . Note that for a circuit QED implementation the modulation of the driving fields can directly control the analog of the proper acceleration with respect to the proper time  $\tau$  (see SM [45]). The detector world line for a general proper acceleration  $a(\tau)$  is (see SM [45] for a derivation)

$$x(\tau) = \int_0^\tau d\tau' \sinh[\xi(\tau')], \quad t(\tau) = \int_0^\tau d\tau' \cosh[\xi(\tau')], \quad (6)$$

where  $\xi(\tau) = \int_0^\tau d\tau' a(\tau')$  is the rapidity [50]. Instead, in the Newtonian case, the (unphysical) world line is simply

$$x_{\text{Newt}}(\tau) = \int_0^\tau d\tau' \xi(\tau'), \quad t_{\text{Newt}}(\tau) = \tau. \quad (7)$$

Each input data point  $\mathbf{x}$  determines a single time evolution of the system  $\hat{\rho}(\tau)$ . We can then measure the detector at times  $\tau_n = n \times \Delta T$  to obtain the expectation values [51] of the quadrature operators  $\hat{q} = (\hat{b} + \hat{b}^\dagger)/\sqrt{2}$ ,  $\hat{p} = i(\hat{b}^\dagger - \hat{b})/\sqrt{2}$  and of the number operator  $\hat{n} = \hat{b}^\dagger \hat{b}$ . The measurements are then collected into a feature vector  $\mathbf{X}$  [see Fig. 1 (e)]. Finally, our trial function reads

$$\hat{f}(\mathbf{x}) = \mathbf{w}^T \mathbf{X}(\mathbf{x}) + b, \quad (8)$$

where the weight  $\mathbf{w}$  and bias  $b$  are parameters to be optimized in order for  $\hat{f}$  to approximate the target function  $f$ . To simplify the notation, in the following we will absorb  $b$  into the vector  $\mathbf{w}$  by appending a constant component 1 to the vector  $\mathbf{X}$ . Due to the linear dependence of the trial function on the feature vector, its optimization can be done analytically.

*Results and discussion.* — As an illustrative example, we consider a non-trivial task: the two-spiral classification problem [52]. The goal is to distinguish two interlocking spiral planar patterns. This task serves as a well-known benchmark for binary pattern classification that is considered hard for multi-layer perceptron models due to its complicated decision boundary [53]. The input data are the two coordinates of each point in the two-spiral pattern  $\mathbf{x} = (x_1, x_2)$ . The task function  $f$  to be learned is such that  $f(\mathbf{x}) = 1$  if the point belongs to the first

spiral branch, and  $f(\mathbf{x}) = -1$  for the other branch [see Fig. 1 (a)]. To train the model, we draw a train dataset of  $N_{\text{train}} = 4000$  sample points  $\{\mathbf{x}_{(1)}, \mathbf{x}_{(2)}, \dots, \mathbf{x}_{(N_{\text{train}})}\}$  with labels  $y_i = f[\mathbf{x}_{(i)}]$  and minimize the regularized least-square loss function. Although most classification problems are commonly treated with other losses [54], the training can be analytically performed under this choice of loss over the training set:

$$\mathcal{L}(\mathbf{w}) = \frac{1}{2N_{\text{train}}} \sum_{i=1}^{N_{\text{train}}} [y_i - \mathbf{w}^T \mathbf{X}(\mathbf{x}_{(i)})]^2 + \frac{l}{2} \|\mathbf{w}\|_2^2, \quad (9)$$

where the last term is a regularization term to prevent overfitting. Denoting  $\Phi$  the matrix whose  $j$ -th column is  $\mathbf{X}(\mathbf{x}_{(j)})$ , and  $\mathbf{y}$  the column vector of the training labels  $y_i$ , the optimal weights are given by  $\mathbf{w}^* = (\Phi \Phi^T + lN_{\text{train}}\mathbb{1})^{-1} \Phi \mathbf{y}$ . The performance of the model is then evaluated on a test sample with  $N_{\text{test}} = 1000$  points. We evaluate the classification accuracy  $\mathcal{A}_{\text{test}}$  on the test set as the fraction of correctly classified samples among  $N_{\text{test}}$ . The training accuracy  $\mathcal{A}_{\text{train}}$ , which indicates how well the reservoir-computing model fits the training set, is defined analogously. The transformation of the input  $\mathbf{x} \mapsto \mathbf{X}(\mathbf{x})$  can be regarded as an embedding of the input from input space into some higher-dimensional feature space. This is best understood by introducing the kernel function [54]  $k(\mathbf{x}, \mathbf{x}') = [\mathbf{X}(\mathbf{x}')]^T \mathbf{X}(\mathbf{x})$ . Under quite general assumptions, this kernel can be diagonalized into an orthonormal [55] set of eigenfunctions  $\{\psi_i\}_i$  with positive eigenvalues  $\{\gamma_i\}_i$  [56]:

$$k(\mathbf{x}, \mathbf{x}') = \sum_i \gamma_i \psi_i(\mathbf{x}) \psi_i(\mathbf{x}'). \quad (10)$$

The set  $\{\psi_i\}_i$  can be completed to be a basis of  $L_\mu^2$  [57] with eigenfunctions associated with  $\gamma_i = 0$ . Note that the kernel spectrum can be empirically computed [58] by calculating the eigenvalues of the matrix  $\Phi \Phi^T / N_{\text{train}}$ . The trial function of Eq. (8) may be rewritten in the above kernel eigenbasis as  $\hat{f}(\mathbf{x}) = \beta^T \psi(\mathbf{x})$  where  $\beta$  is the weight vector to be optimized. The spectrum of the kernel contains crucial information as eigenfunctions with vanishingly small associated eigenvalues do not contribute to the expressivity of the reservoir [40]. In what follows, we will use the kernel spectrum to assess the expressivity of the model.

Throughout our simulations, we fixed the coupling constant to  $\lambda = 0.1$ , the interval of measurement to  $\Delta T = T/2$  and  $\Delta a/a_0 = 0.1$ . The detector's proper frequency is set to be resonant with the third cavity mode [59]  $\Omega = \omega_3$ , the latter being initially in a coherent state  $|\alpha\rangle$  with  $\alpha = 10i$ . We express all quantities in natural units with the scale fixed by  $\Omega$ . The regularization is set to  $l = 10^{-6}$ ; this is equivalent to having a measurement noise of variance  $l$  in the observables [60]. Fig. 2 (a) shows the distribution of testing samples in feature space,

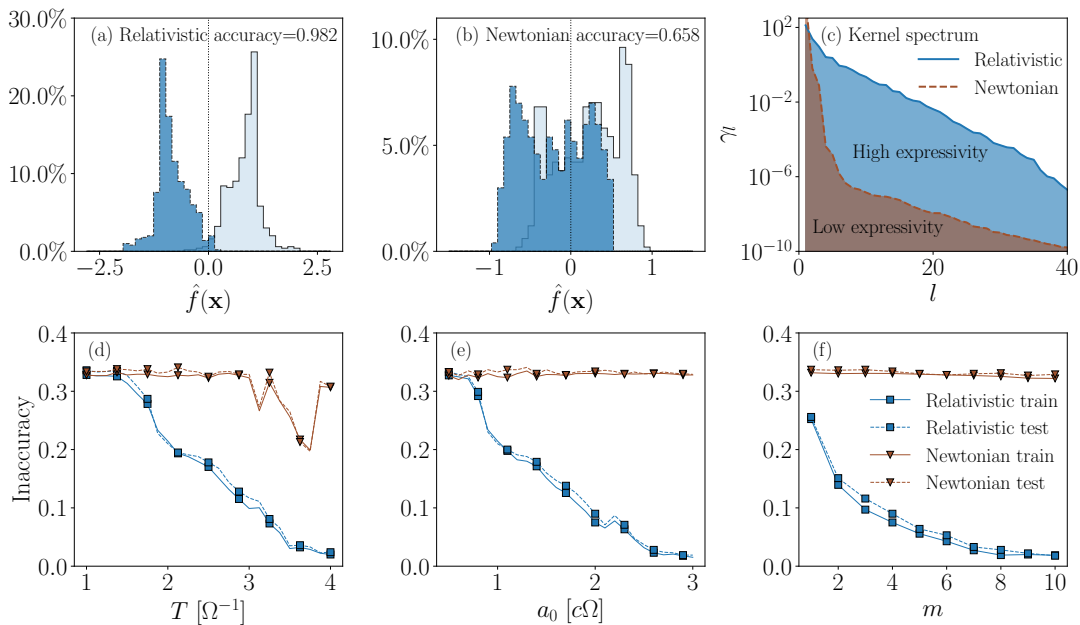


FIG. 2. Figures of merit of the relativistic reservoir-computing protocol. (a) Light and dark histograms correspond to testing samples belonging to different spirals of the dataset. Parameters:  $a_0 = 3$ ,  $T = 2$  and  $m = 4$ . (b) Same quantity plotted for the Newtonian model with same parameters. (c) The empirical kernel spectrum computed for the relativistic (solid line) and Newtonian (dashed line) models with same parameters. The first 40 non-zero eigenvalues  $\gamma_l$  are plotted in descending order. (d) Inaccuracy of the relativistic (triangles) and Newtonian (squares) models evaluated on both the training (solid lines) and testing (dashed lines) set, as a function of the acceleration time  $T$ . Parameters:  $a_0 = 1$  and  $m = 4$ . (e) Same quantities plotted as a function of the base acceleration  $a_0$ , for  $T = 2$  and  $m = 4$ . (f) Same quantities plotted as a function of the number of repetitions  $m$ , for  $a_0 = 2$  and  $T = 2$ . Quantities are expressed in natural units, where the scale is fixed by the proper frequency of the atom  $\Omega$ .

represented by  $\hat{f}(\mathbf{x})$ . The same quantities are plotted in Fig. 2 (b) in a non-relativistic setting, that is, considering Newtonian world lines [Eq. (7)]. As appears from Fig. 2(a) and (b), the relativistic model correctly separates the two classes with high accuracy. By contrast, the system undergoing Newtonian dynamics exhibits a poor performance. The empirical kernel spectra of the two models are plotted in Fig. 2 (c), where we show the first 40 non-zero eigenvalues in descending order. The flatter distribution of the relativistic kernel spectrum implies that for a fixed cutoff threshold on the eigenvalues (or a fixed regularization [40]), it has more eigenfunctions with nonzero eigenvalues that can contribute to the expressivity of the trial function  $\hat{f}$  in comparison with the Newtonian model. Importantly, this relativistically enhanced kernel expressivity associated to the dynamics is *task-independent* and explains the much higher accuracy achieved by the relativistic model for the specific two-spiral classification task.

In Fig. 2 (d), we examine the impact of the acceleration time  $T$  on the performance of the model. As  $T$  increases, the inaccuracy ( $1 - \mathcal{A}$ ) of the relativistic model decreases to around 0, whereas the performance of the Newtonian model remains poor. This is consistent with the results of Fig. 2 (e), where we vary the base acceleration  $a_0$  for

fixed  $T$ . Therein, we also found the inaccuracy of the relativistic model to be decreasing as a function of  $a_0$  as the motion enters the relativistic regime, and a poor performance of the Newtonian model, which remains insensitive to  $a_0$ .

In Fig. 2 (f) we study the effect of the number of repetitions  $m$  of the encoding sequence on the performance. As we are taking measurements at a constant interval  $\Delta T$ , a larger value of  $m$  allows for more features to be collected in the feature vector  $\mathbf{X}$ , improving the efficiency. By contrast, in the Newtonian setting, the supplementary features are close-to-linearly related to the previous ones, thus yielding a negligible improvement. The induced nonlinearity of the feature map associated to the dynamics of the relativistic reservoir ensures that the generated features remain non-trivial after many repetitions. The advantage of the relativistic model can be understood from Eq. (1). Indeed, as discussed in Ref. [6], the phases  $e^{-i[\Omega\tau \pm \omega_n t(\tau)]}$  depend non-trivially on  $\tau$  due to the relativistic (time-dilation) effects, which yields an input-dependent modulation of the cavity-detector resonance condition, absent in the Newtonian model, where one always has  $t_{\text{Newt}}(\tau) = \tau$ .

*Conclusions.*— We have shown how relativistic quantum dynamics can provide a dramatic enhancement of

the expressive power for reservoir computing. Given that analogs of the considered relativistic quantum model can be implemented in state-of-the-art quantum platforms, such as superconducting circuits and trapped ions, our theoretical findings pave the way to relativity-inspired machine-learning protocols with enhanced capabilities.

We acknowledge support by the FET FLAGSHIP Project PhoQuS (grant agreement ID: 820392) and by the French Projects NOMOS (ANR-18-CE24-0026), and TRIANGLE (ANR-20-CE47-0011). We also thank the Ile de France region via the program SIRTEQ. This work was granted access to the HPC resources of TGCC under the allocation A0100512462 attributed by GENCI (Grand Equipement National de Calcul Intensif).

- 
- [1] Asher Peres and Daniel R. Terno, “Quantum information and relativity theory,” *Reviews of Modern Physics* **76**, 93–123 (2004).
- [2] R B Mann and T C Ralph, “Relativistic quantum information,” *Classical and Quantum Gravity* **29**, 220301 (2012).
- [3] David Edward Bruschi, Andrzej Dragan, Antony R. Lee, Ivette Fuentes, and Jorma Louko, “Relativistic motion generates quantum gates and entanglement resonances,” *Phys. Rev. Lett.* **111**, 090504 (2013).
- [4] David Edward Bruschi, Carlos Sabín, Pieter Kok, Göran Johansson, Per Delsing, and Ivette Fuentes, “Towards universal quantum computation through relativistic motion,” *Scientific Reports* **6** (2016), 10.1038/srep18349.
- [5] Samuel L. Braunstein and Peter van Loock, “Quantum information with continuous variables,” *Reviews of Modern Physics* **77**, 513–577 (2005).
- [6] Eduardo Martín-Martínez, David Aasen, and Achim Kempf, “Processing quantum information with relativistic motion of atoms,” *Phys. Rev. Lett.* **110**, 160501 (2013).
- [7] J. R. Johansson, G. Johansson, C. M. Wilson, and Franco Nori, “Dynamical Casimir effect in a superconducting coplanar waveguide,” *Phys. Rev. Lett.* **103**, 147003 (2009).
- [8] Marco del Rey, Diego Porras, and Eduardo Martín-Martínez, “Simulating accelerated atoms coupled to a quantum field,” *Phys. Rev. A* **85**, 022511 (2012).
- [9] S. Felicetti, C. Sabín, I. Fuentes, L. Lamata, G. Romero, and E. Solano, “Relativistic motion with superconducting qubits,” *Phys. Rev. B* **92**, 064501 (2015).
- [10] Alexandre Blais, Arne L. Grimsmo, S. M. Girvin, and Andreas Wallraff, “Circuit quantum electrodynamics,” *Rev. Mod. Phys.* **93**, 025005 (2021).
- [11] L.-M. Duan and C. Monroe, “Colloquium: Quantum networks with trapped ions,” *Rev. Mod. Phys.* **82**, 1209–1224 (2010).
- [12] Gouhei Tanaka, Toshiyuki Yamane, Jean Benoit Héroux, Ryosho Nakane, Naoki Kanazawa, Seiji Takeda, Hidetoshi Numata, Daiju Nakano, and Akira Hirose, “Recent advances in physical reservoir computing: A review,” *Neural Networks* **115**, 100–123 (2019).
- [13] Guy Van der Sande, Daniel Brunner, and Miguel C. Soriano, “Advances in photonic reservoir computing,” *Nanophotonics* **6**, 561–576 (2017).
- [14] Satoshi Sunada, Satoshi Sunada, Kazutaka Kanno, and Atsushi Uchida, “Using multidimensional speckle dynamics for high-speed, large-scale, parallel photonic computing,” *Optics Express* **28**, 30349–30361 (2020).
- [15] Davide Pierangeli, Davide Pierangeli, Davide Pierangeli, Giulia Marcucci, and Claudio Conti, “Photonic extreme learning machine by free-space optical propagation,” *Photonics Research* **9**, 1446–1454 (2021).
- [16] Kristof Vandoorne, Pauline Mechet, Thomas Van Vaerenbergh, Martin Fiers, Geert Morthier, David Verstraeten, Benjamin Schrauwen, Joni Dambre, and Peter Bienstman, “Experimental demonstration of reservoir computing on a silicon photonics chip,” *Nature Communications* **5**, 3541 (2014).
- [17] Florian Denis-Le Coarer, Marc Sciamanna, Andrew Kattumba, Matthias Freiberger, Joni Dambre, Peter Bienstman, and Damien Rontani, “All-Optical Reservoir Computing on a Photonic Chip Using Silicon-Based Ring Resonators,” *IEEE Journal of Selected Topics in Quantum Electronics* **24**, 1–8 (2018).
- [18] Andrzej Opala, Sanjib Ghosh, Timothy C.H. Liew, and Michał Matuszewski, “Neuromorphic Computing in Ginzburg-Landau Polariton-Lattice Systems,” *Physical Review Applied* **11**, 064029 (2019).
- [19] Dario Ballarini, Antonio Gianfrate, Riccardo Panico, Andrzej Opala, Sanjib Ghosh, Lorenzo Dominici, Vincenzo Ardizzone, Milena De Giorgi, Giovanni Lerario, Giuseppe Gigli, Timothy C. H. Liew, Michał Matuszewski, and Daniele Sanvitto, “Polaritonic Neuromorphic Computing Outperforms Linear Classifiers,” *Nano Letters* **20**, 3506–3512 (2020).
- [20] Rafał Mirek, Andrzej Opala, Paolo Comaron, Magdalena Furman, Mateusz Król, Krzysztof Tyszka, Bartłomiej Serebyński, Dario Ballarini, Daniele Sanvitto, Timothy C. H. Liew, Wojciech Pacuski, Jan Suffczyński, Jacek Szczytko, Michał Matuszewski, and Barbara Piętko, “Neuromorphic Binarized Polariton Networks,” *Nano Letters* **21**, 3715–3720 (2021).
- [21] Manjari S. Kulkarni and Christof Teuscher, “Memristor-based reservoir computing,” in *2012 IEEE/ACM International Symposium on Nanoscale Architectures (NANOARCH)* (2012) pp. 226–232.
- [22] Chao Du, Fuxi Cai, Mohammed A. Zidan, Wen Ma, Seung Hwan Lee, and Wei D. Lu, “Reservoir computing using dynamic memristors for temporal information processing,” *Nature Communications* **8**, 2204 (2017).
- [23] Sören Boyn, Julie Grollier, Gwendal Lecerf, Bin Xu, Nicolas Locatelli, Stéphane Fusil, Stéphanie Girod, Cécile Carrétéro, Karin Garcia, Stéphane Xavier, Jean Tomas, Laurent Bellaiche, Manuel Bibes, Agnès Barthélémy, Sylvain Saïghi, and Vincent Garcia, “Learning through ferroelectric domain dynamics in solid-state synapses,” *Nature Communications* **8**, 14736 (2017).
- [24] Ryosho Nakane, Gouhei Tanaka, and Akira Hirose, “Reservoir Computing With Spin Waves Excited in a Garnet Film,” *IEEE Access* **6**, 4462–4469 (2018).
- [25] D. Marković, N. Leroux, M. Riou, F. Abreu Araujo, J. Torrejon, D. Querlioz, A. Fukushima, S. Yuasa, J. Trastoy, P. Bortolotti, and J. Grollier, “Reservoir computing with the frequency, phase, and amplitude of spin-torque nano-oscillators,” *Applied Physics Letters* **114**, 012409 (2019).

- [26] Giulia Marcucci, Davide Pierangeli, and Claudio Conti, “Theory of Neuromorphic Computing by Waves: Machine Learning by Rogue Waves, Dispersive Shocks, and Solitons,” *Physical Review Letters* **125**, 093901 (2020).
- [27] Danijela Marković and Julie Grollier, “Quantum neuromorphic computing,” *Applied Physics Letters* **117**, 150501 (2020).
- [28] Rodrigo Araiza Bravo, Khadijeh Najafi, Xun Gao, and Susanne F. Yelin, “Quantum reservoir computing using arrays of Rydberg atoms,” arXiv e-prints, arXiv:2111.10956 (2021), [arXiv:2111.10956 \[quant-ph\]](https://arxiv.org/abs/2111.10956).
- [29] Sanjib Ghosh, Andrzej Opala, Michał Matuszewski, Tomasz Paterek, and Timothy C. H. Liew, “Quantum reservoir processing,” *npj Quantum Information* **5**, 1–6 (2019).
- [30] Sanjib Ghosh, Andrzej Opala, Michał Matuszewski, Tomasz Paterek, and Timothy C. H. Liew, “Reconstructing Quantum States With Quantum Reservoir Networks,” *IEEE Transactions on Neural Networks and Learning Systems*, 1–8 (2020).
- [31] Sanjib Ghosh, Tomasz Paterek, and Timothy C. H. Liew, “Quantum Neuromorphic Platform for Quantum State Preparation,” *Physical Review Letters* **123**, 260404 (2019).
- [32] Sanjib Ghosh, Tanjung Krisnanda, Tomasz Paterek, and Timothy C. H. Liew, “Realising and compressing quantum circuits with quantum reservoir computing,” *Communications Physics* **4**, 1–7 (2021).
- [33] Tanjung Krisnanda, Sanjib Ghosh, Tomasz Paterek, and Timothy C. H. Liew, “Creating and concentrating quantum resource states in noisy environments using a quantum neural network,” *Neural Networks* **136**, 141–151 (2021).
- [34] Huawen Xu, Tanjung Krisnanda, Wouter Verstraelen, Timothy C. H. Liew, and Sanjib Ghosh, “Superpolynomial quantum enhancement in polaritonic neuromorphic computing,” *Physical Review B* **103**, 195302 (2021).
- [35] Valentin Heyraud, Zejian Li, Zakari Denis, Alexandre Le Boité, and Cristiano Ciuti, “Noisy Quantum Kernel Machines,” arXiv e-prints, arXiv:2204.12192 (2022), [arXiv:2204.12192 \[quant-ph\]](https://arxiv.org/abs/2204.12192).
- [36] Jonathan Dong, Mushegh Rafayelyan, Florent Krzakala, and Sylvain Gigan, “Optical Reservoir Computing Using Multiple Light Scattering for Chaotic Systems Prediction,” *IEEE Journal of Selected Topics in Quantum Electronics* **26**, 1–12 (2020).
- [37] Mushegh Rafayelyan, Jonathan Dong, Yongqi Tan, Florent Krzakala, and Sylvain Gigan, “Large-Scale Optical Reservoir Computing for Spatiotemporal Chaotic Systems Prediction,” *Physical Review X* **10**, 041037 (2020).
- [38] A. Saade, F. Caltagirone, I. Carron, L. Daudet, A. Dreameau, S. Gigan, and F. Krzakala, “Random projections through multiple optical scattering: Approximating Kernels at the speed of light,” *2016 IEEE International Conference on Acoustics, Speech and Signal Processing (ICASSP)* (2016), [10.1109/icassp.2016.7472872](https://doi.org/10.1109/icassp.2016.7472872).
- [39] Ruben Ohana, Jonas Wacker, Jonathan Dong, Sebastien Marmin, Florent Krzakala, Maurizio Filippone, and Laurent Daudet, “Kernel Computations from Large-Scale Random Features Obtained by Optical Processing Units,” in *ICASSP 2020 - 2020 IEEE International Conference on Acoustics, Speech and Signal Processing (ICASSP)* (2020) pp. 9294–9298.
- [40] Zakari Denis, Ivan Favero, and Cristiano Ciuti, “Phononic kernel machine learning for ultrafast spectral analysis,” *Phys. Rev. Applied* **17**, 034077 (2022).
- [41] Eric G. Brown, Eduardo Martín-Martínez, Nicolas C. Menicucci, and Robert B. Mann, “Detectors for probing relativistic quantum physics beyond perturbation theory,” *Phys. Rev. D* **87**, 084062 (2013).
- [42] William G. Unruh and Robert M. Wald, “What happens when an accelerating observer detects a rindler particle,” *Physical Review D* **29**, 1047–1056 (1984).
- [43] Aida Ahmadzadegan, Robert B. Mann, and Eduardo Martín-Martínez, “Measuring motion through relativistic quantum effects,” **90**, 062107.
- [44] R. Simon, E. C. G. Sudarshan, and N. Mukunda, “Gaussian pure states in quantum mechanics and the symplectic group,” *Phys. Rev. A* **37**, 3028–3038 (1988).
- [45] See Supplemental Material at [<link>](#).
- [46] The anharmonicity of a Josephson atom can be made arbitrarily small by replacing a junction by a chain of junctions, as the anharmonicity scales as  $1/N^2$  where  $N$  is the number of junctions.
- [47] Roman Kuzmin, Nitish Mehta, Nicholas Grabon, Raymond Mencia, and Vladimir E. Manucharyan, “Superstrong coupling in circuit quantum electrodynamics,” *npj Quantum Information* **5** (2019), [10.1038/s41534-019-0134-2](https://doi.org/10.1038/s41534-019-0134-2).
- [48] Javier Puertas Martínez, Sébastien Léger, Nicolas Gheeraert, Rémy Dassonneville, Luca Planat, Farshad Foroughi, Yuriy Krupko, Olivier Buisson, Cécile Naud, Wiebke Hasch-Guichard, Serge Florens, Izak Snyman, and Nicolas Roch, “A tunable Josephson platform to explore many-body quantum optics in circuit-QED,” *npj Quantum Information* **5** (2019), [10.1038/s41534-018-0104-0](https://doi.org/10.1038/s41534-018-0104-0).
- [49] Nitish Mehta, Roman Kuzmin, Cristiano Ciuti, and Vladimir E. Manucharyan, “Down-conversion of a single photon as a probe of many-body localization,” arXiv e-prints, arXiv:2203.17186 (2022), [arXiv:2203.17186 \[quant-ph\]](https://arxiv.org/abs/2203.17186).
- [50] Wolfgang Rindler, “Introduction to special relativity. 2,” (1991).
- [51] We assume ensemble measurements for the quantum expectation values.
- [52] Kevin Lang, “Learning to tell two spiral apart,” in *Proceedings of the 1988 connectionist models summer school* (1989) pp. 52–59.
- [53] Chien-Cheng Yu and Bin-Da Liu, “A backpropagation algorithm with adaptive learning rate and momentum coefficient,” in *Proceedings of the 2002 International Joint Conference on Neural Networks. IJCNN’02 (Cat. No.02CH37290)* (IEEE).
- [54] Trevor Hastie, Robert Tibshirani, and Jerome Friedman, *The Elements of Statistical Learning: Data Mining, Inference, and Prediction* (Springer Science & Business Media, 2013).
- [55] With respect to the inner product on  $L^2_\mu$ :  $\langle f, h \rangle \equiv \int f(\mathbf{x})h(\mathbf{x})\mu(d\mathbf{x})$ , where  $\mu(d\mathbf{x})$  denotes the probability distribution of the samples.
- [56] Vern I. Paulsen and Mrinal Raghupathi, *An Introduction to the Theory of Reproducing Kernel Hilbert Spaces*, Cambridge Studies in Advanced Mathematics (Cambridge University Press, Cambridge, 2016).
- [57] The space of square-integrable functions with respect to the probability measure of the input distribution  $\mu(d\mathbf{x})$ .
- [58] Christopher Williams and Matthias Seeger, “Using the

nyström method to speed up kernel machines,” in *Advances in Neural Information Processing Systems 13* (MIT Press, 2001) pp. 682–688.

- [59] This is to ensure that the cavity is long enough for the atom to remain inside. For the circuit QED implementation this is not an important detail.
- [60] Ian Goodfellow, Yoshua Bengio, and Aaron Courville, *Deep Learning*, edited by Francis Bach, Adaptive Computation and Machine Learning Series (MIT Press, Cambridge, MA, USA, 2016).

# Supplementary Material for the article: “Machine learning via relativity-inspired quantum dynamics”

Zejian Li,<sup>1</sup> Valentin Heyraud,<sup>1</sup> Kaelan Donatella,<sup>1</sup> Zakari Denis,<sup>1</sup> and Cristiano Ciuti<sup>1</sup>

<sup>1</sup> *Université Paris Cité, CNRS, Laboratoire Matériaux et Phénomènes Quantiques (MPQ), 75013 Paris, France*

(Dated: May 18, 2022)

In this document, we briefly summarize the Gaussian formalism adopted for calculating the time-evolution of the relativistic quantum system (Section I), the derivation of the detector world line (Section II), the analog implementation of the relativistic model with circuit QED (Section III) and the simulation results with a qubit instead of a harmonic detector (Section IV).

## I. GAUSSIAN FORMALISM FOR THE MODEL WITH A HARMONIC DETECTOR

We denote the vector of bosonic mode operators by

$$\hat{\Psi} = (\hat{a}_0, \hat{a}_1, \hat{a}_2, \dots, \hat{a}_N, \hat{a}_0^\dagger, \hat{a}_1^\dagger, \hat{a}_2^\dagger, \dots, \hat{a}_N^\dagger)^T, \quad (\text{S1})$$

that satisfies the commutation relation

$$\hat{\Psi}_i, \hat{\Psi}_{jt} = \Omega_{ij}, \quad (\text{S2})$$

where

$$\Omega = \begin{bmatrix} \mathbf{0} & \mathbb{1} \\ -\mathbb{1} & \mathbf{0} \end{bmatrix} = -\Omega^T \quad (\text{S3})$$

is the symplectic form. If the Hamiltonian can be written in the form of

$$\hat{H} = \hat{\Psi}^T \mathbf{F}(t) \hat{\Psi}, \quad (\text{S4})$$

it then preserves the Gaussianity of states [S1]. The Heisenberg equations of motion can be written as

$$\frac{d}{dt} \hat{\Psi} = -i\Omega \mathbf{F}^{\text{sym}}(t) \hat{\Psi}, \quad (\text{S5})$$

where  $\mathbf{F}^{\text{sym}} = \mathbf{F} + \mathbf{F}^T$ .

If we define the propagator  $\mathbf{S}(t)$  via the relation

$$\hat{\Psi}(t) = \mathbf{S}(t) \hat{\Psi}(0), \quad (\text{S6})$$

it then satisfies the first order linear differential equation

$$\frac{d}{dt} \mathbf{S}(t) = -i\Omega \mathbf{F}^{\text{sym}}(t) \mathbf{S}(t) \quad (\text{S7})$$

with the initial condition  $\mathbf{S}(0) = \mathbb{1}$ . The evolution of the covariance matrix

$$\sigma_{ij} = \langle \hat{\Psi}_i \hat{\Psi}_j \rangle - \langle \hat{\Psi}_i \rangle \langle \hat{\Psi}_j \rangle \quad (\text{S8})$$

is given by

$$\sigma(t) = \mathbf{S}(t) \sigma(0) \mathbf{S}^T. \quad (\text{S9})$$

$\sigma$  together with  $\langle \hat{\Psi} \rangle$  will completely specify a Gaussian state.

## II. DERIVATION OF THE WORLD LINE

We derive here the world line for an observer with time-dependent proper acceleration  $a(\tau)$  in 1+1D Minkowski spacetime with metric  $\eta_{\mu\nu} = \text{diag}(+1, -1)$ .

We parametrize the world line by the proper time  $x^\mu(\tau) = (t(\tau), x(\tau))$  and denote

$$\begin{aligned} u^\mu(\tau) &= \frac{d}{d\tau} x^\mu(\tau) = (u^t(\tau), u^x(\tau)), \\ a^\mu(\tau) &= \frac{d}{d\tau} u^\mu(\tau) = (a^t(\tau), a^x(\tau)). \end{aligned} \quad (\text{S10})$$

From the definition of these quantities, we get

$$\begin{aligned} u^\mu u_\mu &= 1 = (u^t)^2 - (u^x)^2, \\ a^\mu u_\mu &= 0 = a^t u^t - a^x u^x, \\ a^\mu a_\mu &= -a(\tau)^2 = (a^t)^2 - (a^x)^2. \end{aligned} \quad (\text{S11})$$

It follows that

$$a^x = \frac{du^x}{d\tau} = a(\tau) \sqrt{1 + (u^x)^2}. \quad (\text{S12})$$

Integrating from  $\tau' = 0$  to  $\tau' = \tau$  gives

$$\begin{aligned} u^x(\tau) &= \sinh[\xi(\tau)], \\ \xi(\tau) &= \sinh^{-1}[u^x(\tau = 0)] + \int_0^\tau d\tau' a(\tau'). \end{aligned} \quad (\text{S13})$$

Integrating again gives the position. For the time, a similar treatment applies. We finally obtain:

$$\begin{aligned} x(\tau) &= x_0 + \int_0^\tau d\tau' \sinh[\xi(\tau')], \\ t(\tau) &= t_0 + \int_0^\tau d\tau' \cosh[\xi(\tau')], \end{aligned} \quad (\text{S14})$$

which reduces to the world-line equations in the main text for an observer initially at rest. Note that for a constant acceleration, this gives the well-known Rindler observer's world line.

## III. IMPLEMENTATION WITH CIRCUIT QED

We present a potential implementation of the proposed relativistic model on circuit QED platforms inspired by [S2], which consists of a Josephson artificial atom with bosonic mode operator  $\hat{b}$  (simulating the harmonic oscillator described in the main text) coupled to a microwave



cavity in the strong-coupling regime. Denoting the microwave cavity mode operator by  $\hat{a}$ , the noninteracting Hamiltonian of the system is

$$\hat{H}_0(\tau) = \omega_0 \hat{a}^\dagger \hat{a} + \epsilon \hat{b}^\dagger \hat{b} + \eta \zeta(\tau) \hat{b}^\dagger \hat{b}, \quad (\text{S15})$$

where  $\omega_0$  is the cavity bare frequency,  $\epsilon$  is the energy of the artificial atom, and we assumed that the Josephson junction has negligible nonlinearity. This can be achieved for example by replacing a single Josephson junction with a sufficiently long chain of junctions. The opposite extreme case, where the Josephson atom is a two-level system (qubit), yields similar results, as revealed by corresponding simulations reported in Section IV.  $\zeta(\tau)$  is a driving function that takes the following form [S3]:

$$\begin{aligned} \zeta(\tau) &= \frac{d}{d\tau} F(\tau), \\ F(\tau) &= F_+(\tau) + F_-(\tau), \end{aligned} \quad (\text{S16})$$

where

$$F_\pm = \cos[\omega_\pm \tau \mp \theta_\mp(\tau)] - \cos[\omega_\pm \tau \mp \theta_\pm(\tau)]. \quad (\text{S17})$$

Assuming that the phases  $\theta_\pm(\tau)$  are modulated slowly compared to the driving frequencies  $\omega_\pm$ , as will indeed be the case in what follows, the driving function  $\zeta(\tau)$  can be well approximated by

$$\begin{aligned} \zeta(\tau) &\simeq -\omega_+ \sin[\omega_+ \tau - \theta_-(\tau)] \\ &\quad + \omega_+ \sin[\omega_+ \tau - \theta_+(\tau)] \\ &\quad - \omega_- \sin[\omega_- \tau + \theta_+(\tau)] \\ &\quad + \omega_- \sin[\omega_- \tau + \theta_-(\tau)]. \end{aligned} \quad (\text{S18})$$

The interaction Hamiltonian in the Schrödinger picture is  $\hat{H}_I = g(\hat{b}^\dagger + \hat{b})(\hat{a} + \hat{a}^\dagger)$ . Passing to the interaction picture with respect to  $\hat{H}_0(\tau)$  and assuming  $\eta \ll 1$  in the driving term, we get

$$\begin{aligned} \hat{H}_I(\tau) &= g[\hat{b}^\dagger e^{i\epsilon\tau} \mathcal{G}(\tau) + \text{H.c.}](\hat{a} e^{-i\omega_0\tau} + \text{H.c.}), \\ \mathcal{G}(\tau) &= e^{i\eta F(\tau)} \simeq 1 + i\eta F(\tau). \end{aligned} \quad (\text{S19})$$

To simulate a harmonic oscillator with proper frequency  $\Omega$  and world line  $x^\mu(\tau) = (t(\tau), x(\tau))$  coupled to the  $n$ th mode of a massless scalar field of frequency  $\omega_n = k_n$  as considered in the main text, we now choose  $\omega_\pm = \epsilon \pm \omega_0 - \Omega$  as the driving frequencies and  $\theta_\pm(\tau) = \omega_n t(\tau) \pm k_n x(\tau)$  as the phase modulations. In the regime where  $\epsilon, \omega_0, |\epsilon \pm \omega_0| \gg g$ , the interaction Hamiltonian becomes (keeping only slowly rotating terms)

$$\begin{aligned} \hat{H}_I(\tau) &\simeq g\eta \sin[k_n x(\tau)] \times \\ &\quad \hat{b}(\hat{a} e^{-i[\Omega\tau + \omega_n t(\tau)]} + \hat{a}^\dagger e^{-i[\Omega\tau - \omega_n t(\tau)]}) + \text{H.c.}, \end{aligned} \quad (\text{S20})$$

which takes the form of the interaction Hamiltonian in the main text for a single mode of the quantum field. Note that since we always consider a single-mode coherent state as the field initial state in the main text, the

main contribution to the dynamics of the harmonic oscillator comes uniquely from this mode, as one can verify using perturbation theory [S4]. We also checked numerically that a single-mode approximation for the quantum field is enough for obtaining accurate results for the simulations presented in the main text. Nonetheless, it is possible to simulate the full many-mode Hamiltonian by using multiple modes in the circuit QED microwave cavity.

As considered in [S2], the energy scales  $\epsilon$  and  $\omega_0$  for circuit QED are in the GHz regime, while  $g, \Omega$  and  $\omega_n$  can be on much slower time scales, such as in the MHz regime. The modulation rate of the phases  $\dot{\theta}_\pm(\tau)$  can be expressed in terms of the simulated time-dependent acceleration  $a(\tau)$  as [using the world line in Eq. (S14)]

$$\begin{aligned} \dot{\theta}_\pm(\tau) &= \frac{d}{d\tau} [\omega_n t(\tau) \pm k_n x(\tau)] \\ &= \omega_n \cosh[\xi(\tau)] \pm k_n \sinh[\xi(\tau)] \\ &= \omega_n \cosh \left[ \int_0^\tau d\tau' a(\tau') \right] \pm k_n \sinh \left[ \int_0^\tau d\tau' a(\tau') \right]. \end{aligned} \quad (\text{S21})$$

Let us consider a typical world line studied in the main text, for example with  $a_0 = 2, \Delta a/a_0 = 0.1, T = 2$  and  $\omega_n = \Omega$  [the values used in Fig. 2(f) of the main text] in the units fixed by  $\Omega$ . Then, we have  $\dot{\theta}_\pm(\tau) \lesssim 10\Omega$ , meaning that the phases in the driving (S17) need to be modulated at roughly the same timescale as  $\Omega$ , in the MHz band, which is much slower than the circuit QED timescales and should be experimentally feasible.

Finally, let us consider a concrete example of typical parameter values of the analog circuit QED system. Let the parameters of the system be  $\omega_0 = 1$  GHz,  $\epsilon = 1.1$  GHz,  $\Omega = 1$  MHz,  $g = 10/\sqrt{3\pi}$  MHz  $\simeq 3.3$  MHz,  $\eta = 0.01$ . The driving frequencies are then  $\omega_+ = 2.099$  GHz and  $\omega_- = 0.099$  GHz. This simulates the harmonic detector coupled to the  $n = 3$  mode of the quantum field (with  $\Omega = \omega_n = k_n$  and  $\lambda = 0.1$ ) as considered in the main text. To simulate the acceleration sequence described in the main text in the case of  $a_0 = 2, \Delta a/a_0 = 0.1$  and  $T = 2$ , the required phase modulations  $\theta_\pm(\tau)$  as well as their rates  $\dot{\theta}(\tau)$ , given by Eq. (S21), are plotted in Fig. S1.

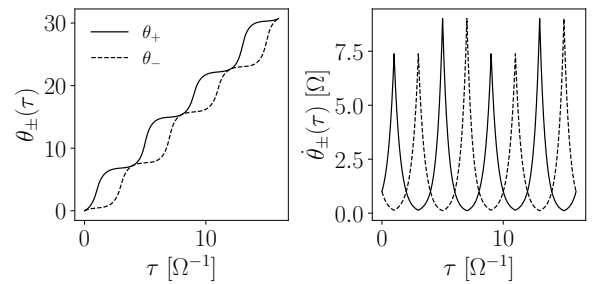


FIG. S1. The phase modulations  $\theta_\pm(\tau)$  (left panel) and the corresponding rates  $\dot{\theta}_\pm(\tau)$  that provide the desired simulation of the accelerated motion, where  $\Omega = 1$  MHz. Note that modulation rates are in the regime of  $\dot{\theta}_\pm(\tau) \lesssim 10\Omega = 10$  MHz.

#### IV. RESULTS WITH A QUBIT INSTEAD OF A HARMONIC OSCILLATOR

We report here the simulation results when we replace the harmonic detector with a qubit (two-level atom initially in its ground state) for the same parameters considered in the main text. To model the configuration with the qubit, we have to replace the bosonic mode operator  $\hat{b}$  with the Pauli operator  $\hat{\sigma}^-$  in the Hamiltonian. Since the Gaussian formalism can no longer be applied, we assumed a single-mode approximation for the quantum field (considering only the mode that is initially in the coherent state and in resonance with the proper frequency of the qubit), which matches the exact form of the single-mode circuit-QED Hamiltonian in Eq. (S20). The feature vector now contains the expectation values of the operators that are respectively analogous to the bosonic occupation number and the quadratures, namely  $\hat{\sigma}^+\hat{\sigma}^-$ ,  $(\hat{\sigma}^- + \hat{\sigma}^+)/\sqrt{2}$  and  $i(\hat{\sigma}^+ - \hat{\sigma}^-)\sqrt{2}$ . This is equivalent to measuring the Pauli operators  $\hat{\sigma}^z$ ,  $\hat{\sigma}^x$  and  $\hat{\sigma}^y$  respectively. The equivalent of Fig. 2(d) and (e) in the main text are presented in Fig. S2(a) and (b) for the qubit model. We recover results similar to the case of the harmonic detector. Note that the Newtonian model has a

slightly improved, yet still very poor performance, which can be ascribed to the additional nonlinearity provided by the qubit. These results clearly show that the details of the spectrum of the detector are not crucial for the expressive power of the relativistic quantum dynamics.

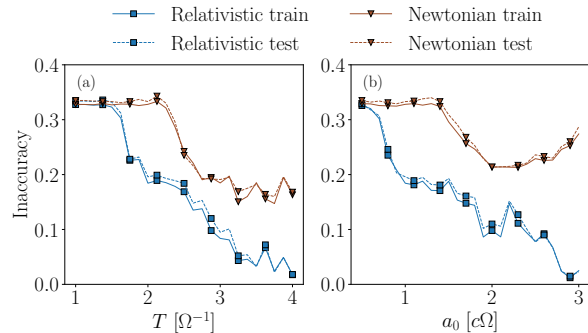


FIG. S2. Performances of the reservoir-computing model considered in the main text, but with a qubit replacing the harmonic oscillator. Same parameters as Fig. 2(d) and (e) in the main text respectively, showing very similar results.

- 
- [S1] R. Simon, E. C. G. Sudarshan, and N. Mukunda, Gaussian pure states in quantum mechanics and the symplectic group, *Phys. Rev. A* **37**, 3028 (1988).
- [S2] M. del Rey, D. Porras, and E. Martín-Martínez, Simulating accelerated atoms coupled to a quantum field, *Phys. Rev. A* **85**, 022511 (2012).

- [S3] Note that our driving term is different from that in [S2], as they considered simulating a quantum field in free space, while in the present work, the simulated quantum field is confined within a cavity with Dirichlet boundary conditions, resulting in different mode functions.
- [S4] E. Martín-Martínez, D. Aasen, and A. Kempf, Processing quantum information with relativistic motion of atoms, *Phys. Rev. Lett.* **110**, 160501 (2013).